NANO LETTERS

LETTER

pubs.acs.org/NanoLett

Mapping Nanomagnetic Fields Using a Radical Pair Reaction

Hohjai Lee,[†] Nan Yang,[‡] and Adam E. Cohen*[,†,§]

[†]Department of Chemistry and Chemical Biology, [‡]School of Engineering and Applied Sciences, and [§]Department of Physics, Harvard University, Cambridge, Massachusetts 02138, United States

Supporting Information

ABSTRACT: We used a fluorescent chemical indicator of magnetic field to visualize the magnetic field around ferromagnetic nanostructures. The indicator was a chain-linked electron donor−acceptor molecule, phenanthrene-$(CH_2)_{12}$-O-$(CH_2)_2$-dimethylaniline, that forms spin-correlated radical pairs upon photoexcitation. The magnetic field altered the coherent spin dynamics, yielding an 80% increase in exciplex fluorescence in a 0.1 T magnetic field. The magnetic field distributions were quantified to precision of 1.8×10^{-4} T by image analysis and agreed with finite-element nanomagnetic simulations.

KEYWORDS: Magnetic field effect, radical pair, fluorescence microscopy, magnetic nanostructure, intersystem crossing

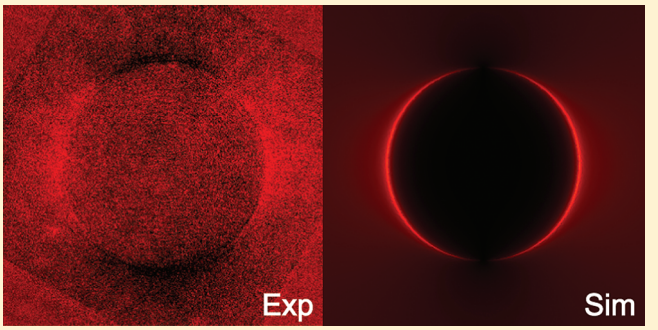

Magnetic micro- and nanostructures are expected to play an increasingly important role in spin-based computation and data storage devices.[1,2] Programmable magnetization patterns have been proposed as tools for manipulating microscopic objects, e.g., cells and particles, on surfaces.[3,4] However, there is a need for improved techniques to map the magnetic field around such structures, particularly in complex three-dimensional geometries. The traditional technique of Bitter imaging probes magnetic gradients above planar substrates but is not quantitative and leaves a residue of particles on the surface.[5] Scanning techniques such as magnetic force,[6,7] Hall effect,[8] and SQUID microscopy[9] are exquisitely sensitive but are slow and require quasi-planar substrates. Magneto-optic Kerr effect (MOKE) imaging[10] provides wide-field contrast but only probes surface magnetization and also requires a planar substrate to provide specular reflection of the probe laser. Nitrogen vacancy (N−V) defects in diamond were recently used to perform highly sensitive vector magnetometry around fabricated nanostructures,[11,12] but the technique required integration of the diamond magnetometer with the sample and thus could not probe complex three-dimensional structures. Here we demonstrate mapping of the magnetic field around magnetic nanostructures using a combination of fluorescence microscopy and a chemical indicator whose fluorescence is sensitive to the magnetic field strength. This technique provides three-dimensional imaging of the field strength, does not disrupt the sample, and requires only a simple optical imaging system.

Magnetically sensitive chemical reactions are a dramatic example of quantum coherence under ambient conditions.[13,14] The interaction energy of a 10 mT magnetic field with an electron spin is less than $k_BT/400$ at room temperature, and thus one might expect magnetic fields to have negligible influence on chemical reactions. However, in certain photochemical processes, the outcome is determined largely by coherent spin dynamics rather than by thermodynamics.

In chemical systems showing a magnetic field effect (MFE), photoinduced electron transfer generates a radical pair (RP) in which the electrons are initially in an entangled spin state, yet are distant enough to be only weakly interacting. The electron spins evolve, each under the influence of the local magnetic interactions. Hyperfine couplings to nearby magnetically active nuclei (mostly ^{1}H, ^{14}N, and ^{13}C) induce differential precession of the electron spins and thus favor intersystem crossing (ISC). An external magnetic field induces an electronic Zeeman splitting of the T_+ and T_- states. Very small magnetic fields can enhance ISC through the "low field effect",[15] while larger magnetic fields decouple the T_+ and T_- states from the singlet and thereby suppress ISC. Even larger fields can again enhance ISC if the two electrons have different g values.

If the radical-bearing moieties later reencounter, the outcome depends on the symmetry of the spin wave function: a spin triplet mandates a spatially antisymmetric wave function, while a spin singlet mandates a symmetric wave function. The differing symmetries of the spatial wave function lead to different reaction pathways. A modern treatment of magnetic field effects in radical pair reactions is given in ref 16.

Spin-correlated radical pairs are important in polymer chemistry,[17] organic chemistry,[18,19] material science,[20] and photosynthesis.[21,22] Magnetic field effects on spin-correlated radical pairs have been proposed as the primary transduction mechanism in the magnetic sense of birds and insects, although this

Received: August 24, 2011
Revised: October 31, 2011

ACS Publications © XXXX American Chemical Society

dx.doi.org/10.1021/nl202950h | *Nano Lett.* XXXX, XXX, 000–000

hypothesis has not been confirmed by direct measurements on the putative sensor cryptochrome proteins.[23]

Here we use a photochemical RP reaction in which the singlet product is a fluorescence photon. The MFE on fluorescence is measured by

$$\mathrm{MFE} = \frac{F_B - F_0}{F_0} \quad (1)$$

where F_B and F_0 represent the fluorescence intensity in finite and zero applied magnetic field, respectively. Exciplex fluorescence of the electron transfer couple pyrene/*N*,*N*-dimethylaniline (Py/DMA) is well-known to depend on magnetic field,[24] with saturating MFEs as large as 18% in mixed solvent systems.[25] Yang and Cohen recently used fluorescence of Py/DMA to perform a new type of imaging, termed magneto-fluorescence imaging (MFI),[26] which could image through strongly scattering media, such as frosted glass. However, due to the delicate interplay of reencounter rates and spin evolution in Py/DMA, the magnitude of the MFE was very sensitive to solvent dielectric constant and polarity,[27,28] which limited the utility of MFI.

Tethering the donor and acceptor by an inert linker increases the probability of geminate reencounter and enhances the magnitude of the MFE.[24] In the present experiment we used a chain-linked donor−acceptor molecule (phenanthrene−$(CH_2)_{12}$−O−$(CH_2)_2$−DMA (**1**), Figure 1a), which was previously reported to show magnetic field effects as large as 140%.[29] The mechanism of the MFE in this molecule has previously been analyzed in detail.[30]

Experiment. Compound **1** was synthesized in two steps following a published procedure.[29,30] The first reaction yielded the intermediate Phen−$(CH_2)_{12}$−Br, and the second reaction yielded the final product (**1**). We modified the procedures in refs 29 and 30 as follows. For both reactions, we used ether instead of benzene to extract the products. For the second reaction, after extraction with ether, we added HCl to neutralize the NaH until the pH reached 7. The sample was then washed with distilled water. All fluorescence measurements of **1** were performed in *N*,*N*-dimethyl formamide (DMF). Oxygen quenched the fluorescence, so solutions were deoxygenated by bubbling with N_2 (99.999%) for 15 min prior to each measurement. A peristaltic pump maintained a continuous flow of solution of **1** (5×10^{-4} M) in degassed DMF during the experiments. The flow maintained a low oxygen concentration in the imaging volume and replaced indicator molecules that had photobleached.

We fabricated various shapes of iron nanostructures on a Si wafer using photolithography, thermal deposition of a Cr adhesion layer (10 nm) followed by Fe (700 nm), and liftoff. The sample was mounted in an imaging chamber which maintained a thin film of magnetic indicator solution in contact with the sample (Figure 1b). To minimize background fluorescence from indicator molecules far from the sample, we used the technique of convex lens-induced confinement (CLIC) to create a nanoscale film of indicator solution.[31] A plano-convex lens (f = 100 mm) was placed convex side down, contacting the sample at a single point. By selecting an imaging region at a known distance from the point of contact, we could select an arbitrary thickness of indicator solution. Typically we imaged at a solution depth of <100 nm above the nanofabricated structures. The sample cell provided optical access through the convex lens.

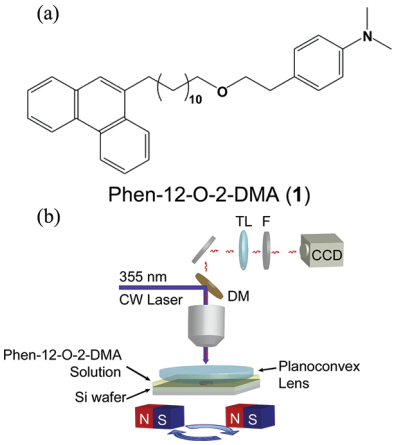

Figure 1. Apparatus for mapping nanomagnetic fields. (a) Molecular structure of the fluorescent magnetic field indicator, phenanthrene−$(CH_2)_{12}$−O−$(CH_2)_2$−DMA (**1**). (b) Imaging system. A planoconvex lens confined the indicator solution to a nanoscale film above the surface of a sample containing planar iron nanostructures. A pair of magnets mounted below the sample generated an in-plane magnetic field that could be rotated about the optical axis. DM, dichroic mirror; TL, tube lens; F, emission filter.

A 355 nm continuous wave laser (Opto Engine LLC, 2.5 mW) illuminated the sample via a home-built epifluorescence microscope with a 40× UV objective (Olympus, LUCPlanFLN). The exciplex fluorescence was separated from illumination light by a dichroic mirror (Olympus, U-MWU2, cutoff at 400 nm) and an emission filter (Chroma, 500−700 nm band-pass). Images were collected on an electron-multiplying CCD camera (Andor iXon$^+$ 897).

Two NdFeB permanent magnets, each a 1 cm cube, were mounted beneath the sample as shown in Figure 1b. The magnetic field lay in the plane of the sample, and its orientation was set by rotating the magnet assembly on a motorized rotation stage (Thorlabs, PRM1-Z7). To determine the strength of the applied magnetic field, we replaced the sample with the sensor of a Hall magnetometer. The spacing between the magnets and the sample was adjusted to set the local field strength within the range of maximum sensitivity of the fluorescent indicator (8 mT < B < 15 mT). The applied field was parallel to the plane of the sample, with a magnitude $B^{(0)}$ = 8.3 mT. This value was not sensitive to the microscopic location of the Hall probe because the applied field in the sample plane was homogeneous on the scale of the Hall Probe ($1.5 \times 3 \times 4$ mm).

Fluorescence images were collected at different in-plane orientations of the applied field, with steps of 60° for circle and triangle structures and 45° for a square structure. The magnets were rotated through all orientations 30 times, with 1 s exposures at each orientation.

To demonstrate magnetic mapping around a complex three-dimensional object, we also studied a ∼120 μm diameter irregularly shaped grain of iron, adhered to a Si wafer by a thin film of sodium silicate. The magnetic indicator used in this experiment was a solution of Py (10^{-4} M)/DMA (5×10^{-2} M) in 3:1 tetrahydrofuran (THF):DMF and was illuminated by UV light from a mercury lamp with a 350 nm short-pass filter (Asahi XUS0350).

We simulated the magnetic field distribution around each nanostructure using finite-element analysis with COMSOL

dx.doi.org/10.1021/nl202950h |*Nano Lett.* XXXX, XXX, 000–000

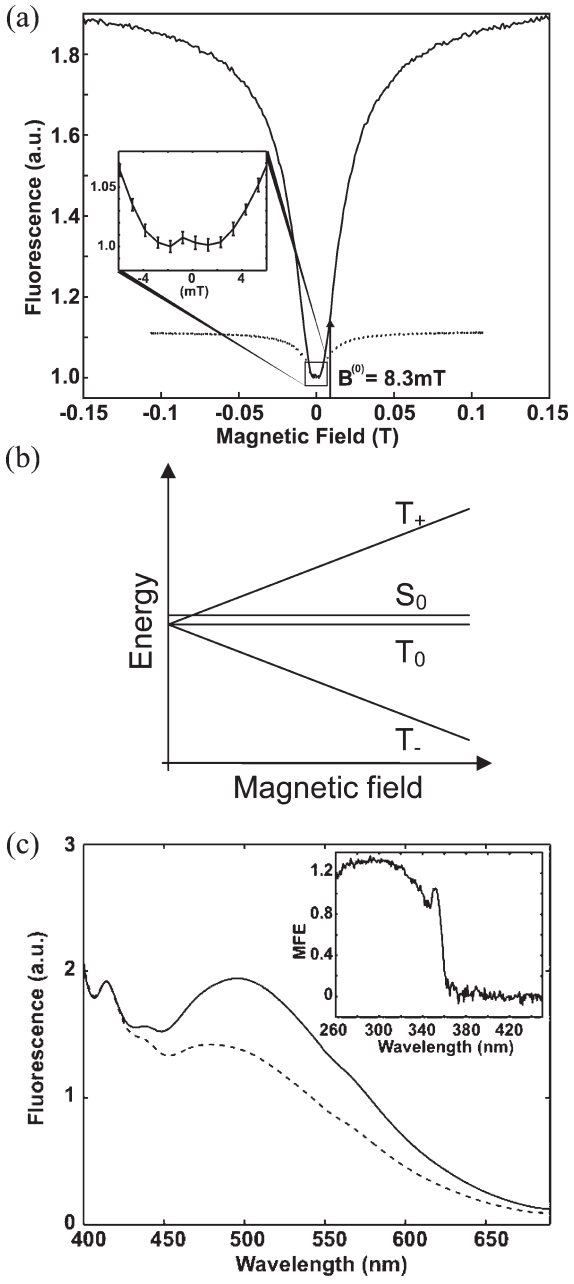

Figure 2. Photophysical properties of the fluorescent magnetic field indicator (**1**). (a) Fluorescence as a function of magnetic field (points). The solid line is a linear interpolation of the points. Imaging experiments were conducted at an applied field strength of $B^{(0)}$ = 8.3 mT, indicated by arrow. The exciplex fluorescence from unchained Py/DMA is also plotted for comparison (dotted line). Inset: fluorescence of (**1**) near zero field. (b) Energy level diagram showing the alignment of the T_+ and S_0 states at low magnetic field and breaking of the near degeneracy at high magnetic field. (c) Magnetic field dependent emission spectrum with 355 nm excitation (solid line, B = 50 mT. dashed line, B = 0). Inset: Magnetic field effect on exciplex fluorescence at 525 nm as a function of excitation wavelength.

Multiphysics, using the tabulated permeability of Fe and a mesh with a minimum element size of 200 nm.

Results. Figure 2a shows the exciplex fluorescence of **1** as a function of applied magnetic field, under illumination at 355 nm. The compound showed an 80% increase in exciplex fluorescence upon application of a magnetic field of 0.1 T. The fluorescence reached to half of its saturating value at a field $B_{1/2}$ = 19.5 mT. At low magnetic field, $B \sim 2$ mT, the fluorescence showed a small dip. This dip was absent in the unchained phenanthrene/DMA exciplex and was strongly enhanced in chained phenanthrene–DMA compounds with shorter tethers, suggesting that the dip was due to exchange coupling in the radical pair.[29] Figure 2b shows that in the presence of finite exchange interaction, a small magnetic field of induces a degeneracy of the T_+ and S_0 states, leading to enhanced ISC and decreased fluorescence, while a larger magnetic field breaks the degeneracy, leading to decreased ISC and enhanced fluorescence. No efforts were made to null the ambient Earth field, and so the possibility of a "low field effect"[15] near B = 0 was not addressed.

Figure 2c shows the emission spectrum of **1** with and without an applied magnetic field. The prompt fluorescence from the phenanthrene (370–450 nm) did not vary with magnetic field, but the exciplex fluorescence (500–700 nm) was exquisitely sensitive to magnetic field. The inset of the Figure 2c shows the MFE measured at 525 nm as a function of excitation wavelength. The MFE reached to more than 80% with UV excitation shorter than 360 nm and peaked at 308 nm with an MFE of 130%. The existence of a large MFE with excitation at 355 nm made compound **1** favorable for imaging with laser illumination. Under UV illumination, bringing a permanent magnet up to a solution of **1** led to an increase in fluorescence which was readily visible by eye (Supporting Movie 1, Supporting Information).[32]

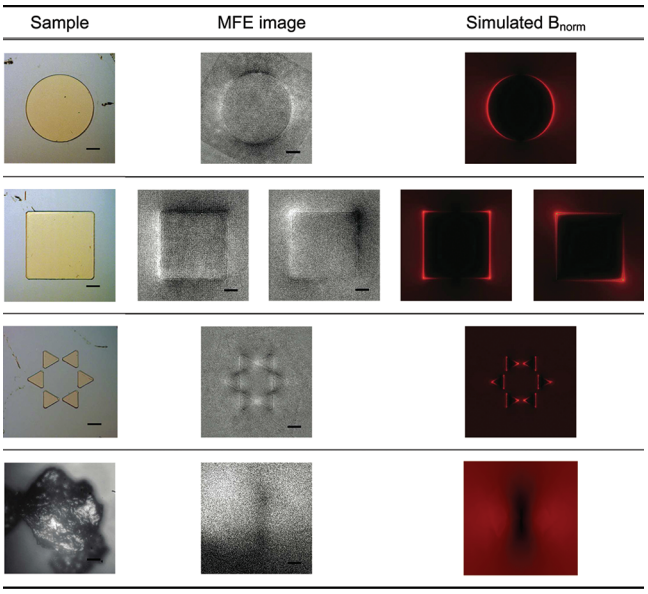

Figure 3. Maps of magnetic field strength around nano- and microstructures. First column: White light images. Second column: MFE images. Third column: Simulated magnetic flux density. The external magnetic field is applied in horizontal direction (θ = 0°), except for the second MFE image of the square structure with θ = 45°. Scale bars 20 μm. The color scale for the simulated field of the sphere is half that of the others.

Figure 3 shows in the left column the iron nanostructures used in the experiment. The applied magnetic field induced magnetization of these structures, leading to local field inhomogeneities. These inhomogeneities led to spatially varying fluorescence from the indicator solution. As the magnetic field rotated, the fluorescence emission pattern rotated too.

dx.doi.org/10.1021/nl202950h |*Nano Lett.* XXXX, XXX, 000–000

Images were analyzed as follows. Let $I^{(0)}(\theta)$ represent the image acquired at field orientation θ. To correct for laser intensity fluctuations, each image was divided by its average brightness

$$I(\theta) = I^{(0)}(\theta)/\langle I^{(0)}(\theta)\rangle_{x,y}$$

where $\langle\ \rangle_{x,y}$ indicates a single number equal to the fluorescence averaged over the entire image. An image of the fractional change in fluorescence at each magnet orientation was then calculated by

$$\mathrm{MFE}(\theta) = \frac{I(\theta) - \langle I(\theta)\rangle_\theta}{\langle I(\theta)\rangle_\theta}$$

where the subtraction and division operations were performed pixel by pixel and $\langle I(\theta)\rangle_\theta$ indicate an image obtained by averaging the fluorescence images over all magnetic field orientations. In the image $\langle I(\theta)\rangle_\theta$, the orientation-dependent contributions to the fluorescence have been averaged out. To enhance the signal-to-noise ratio, MFE images related by a symmetry operation (e.g., rotated by 90° for the square) were rotated to the same orientation and averaged together. The middle column of Figure 2 shows these results, in which the fluorescence is noticeably brighter in the high-field regions and dimer in the low-field regions.

The images in the third column of Figure 3 show the simulated magnetic flux density B evaluated 100 nm above the top surface of the structures. The relative permeability values were $\mu_r = 5000$ for the iron and $\mu_r = 1$ for the surrounding indicator solution, and a remnant flux density $B_r = 8.3$ mT was applied in the horizontal direction ($\theta = 0°$). The iron grain in the bottom row was approximated as a sphere and the magnetic field was evaluated 100 nm above the top of the sphere.

Discussion. Planar nanostructures showed enhanced fluorescence along the edges perpendicular to the applied field, indicating that along these edges the induced field enhanced the applied field. The edges parallel to the applied field showed decreased fluorescence, indicating that the induced fringing fields partially canceled the applied field. The hexagram of equilateral triangles showed particularly strong field enhancement at junctions between vertices aligned parallel to the field, similar to optical field enhancements in bowtie nanoantennas.[33]

The nonplanar iron microparticle also showed a magnetic field-dependent modification of the fluorescence, with a dark band appearing in the middle of the structure, perpendicular to the applied field. Along the equator of the particle, the fringing fields were oriented oppositely to the applied field, while at the poles the fringing fields were parallel to the applied field. A numerical simulation of a sphere in an external field reproduced this simple banding pattern. This result demonstrates magnetic field mapping in a complex geometry that would be difficult to probe by conventional means.

To demonstrate quantitative magnetic field mapping, we converted the fluorescence images into images of field strength, using the MFE curve in Figure 2a. The applied magnetic field, $B^{(0)}$, previously measured with a Hall magnetometer, set the boundary conditions in regions of the sample far from the magnetic nanostructure. Magnetic field dependent variations in fluorescence intensity were only ~1% of the average fluorescence at the boundaries, implying that the variations in magnetic field were small compared to $B_{1/2}$. Thus within the range of magnetic fields in the sample, the MFE curve could be approximated by a Taylor series around $B = B^{(0)}$: $F(B) \approx F(B_0) + (B - B_0)(\mathrm{d}F/\mathrm{d}B)_{B=B^{(0)}}$. Rearranging

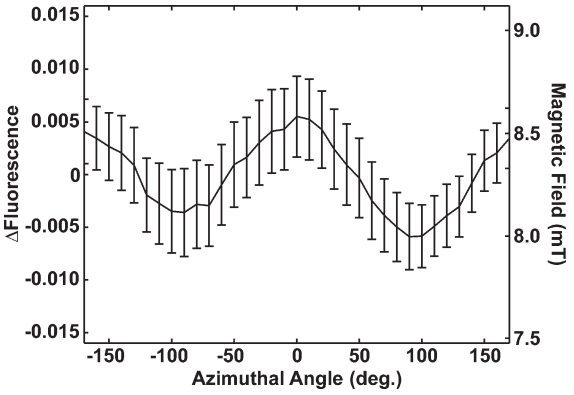

Figure 4. The azimuthal distributions of MFE (left y axis) and magnetic field (right y axis) around the 100 μm diameter circular iron structure. External magnetic field is in horizontal direction ($\theta = 0°$).

and substituting the definition of the MFE (eq 1) yields

$$B \approx B^{(0)} + \mathrm{MFE}\left(\frac{\mathrm{d}(\mathrm{MFE})}{\mathrm{d}B}\right)^{-1}\Bigg|_{B=B^{(0)}} \quad (2)$$

Equation 2 was used pixel by pixel to calculate the local magnetic field. The calculated variation in magnetic field strength around the circular structure was 0.5 mT, well within the range of the linear approximation of eq 2. For structures that generate large variations in the local magnetic field, one should use the complete MFE curve to create a lookup table, rather than relying on eq 2.

Focusing on the circular structure, we quantified the fluorescence as a function of angle in an annulus extending 13 μm from the edge of the structure. Figure 4 shows the angular distribution of the MFE. As expected, the MFE values were maximum at 0° and 180° and minimum at 90° and −90°. The maximum MFE was ~1.7% (Figure 4). We used eq 2 to convert the MFE measurements into field estimates. The precision of our estimates of field strength is 1.78×10^{-4} T, dominated by low-frequency drift in the apparatus.

While one may take the MFE curve plotted in Figure 2a as an empirical fact, it is useful to consider the physical processes that contribute to this curve. The MFE of related compounds with varying chain length has previously been explored in detail.[29,30] Photoexcitation of **1** generates a spin-correlated radical pair in an initial singlet state. The singlet radical pair can recombine to generate fluorescence or it can undergo ISC to the triplet state, which is not fluorescent. The branching ratio between singlet and triplet pathways depends on the extent of ISC during the lifetime of the radical pair. Electron−nuclear hyperfine interactions drive ISC, provided that the energy gap between the singlet and a triplet level is less than the mean hyperfine coupling. Figure 2b shows that, in the presence of weak exchange coupling, a small magnetic field induces degeneracy of the T_+ and S_0 levels, while a stronger magnetic field breaks this degeneracy.

Weller and co-workers showed that the effective hyperfine field on electron i (=1, 2) is

$$B_i = \left(\sum_k a_{ik}^2 I_k(I_k + 1)\right)^{1/2}$$

where a_{ik} is the isotropic nuclear hyperfine coupling constant between electron i and nucleus k and I_k is the spin of nucleus k.[34] The sum runs over all the nuclei on the molecule containing the

dx.doi.org/10.1021/nl202950h |Nano Lett. XXXX, XXX, 000–000

radical pair. In the absence of exchange coupling, the value of the external field, $B_{1/2}$, at which the MFE is at half its saturation value is approximately

$$B_{1/2} = \frac{2({B_1}^2 + {B_2}^2)}{B_1 + B_2}$$

Weller and co-workers found good agreement between their formula and experiments with unchained Py/DMA.

Using the tabulated values of the hyperfine constants for phenanthrene and DMA,[34] the Weller formula predicts a value for $B_{1/2}$ = 5.5 mT. However, for the chained compound **1** we measured $B_{1/2}$ = 19.5 mT. This discrepancy arises because exchange coupling enhances the magnitude of the applied field necessary to decouple the T_+ state from S_0 (Figure 2b). The MFE curve for unchained phenanthrene/DMA was in closer accord with the prediction of the Weller formula. The shape of the MFE curve for **1** is consistent with the chain-length-dependent trend identified by Cao and co-workers.[29] We do not expect paramagnetic ions released from the iron nanostructures to contribute to the MFE because such ions would have negligible solubility in DMF. The concentration of **1**, 5×10^{-4} M, would vastly exceed the concentration of any paramagnetic impurities.

Conclusion. We demonstrated that magnetic control of coherent spin dynamics in a room-temperature liquid enables quantitative optical mapping of magnetic fields around complex two- and three-dimensional magnetic structures. We used wide-field epifluorescence coupled with convex-lens-induced confinement for imaging, but our results readily generalize to other optical imaging schemes. For instance one could use one-photon or two-photon confocal fluorescence to achieve true three-dimensional profiling. Total internal reflection fluorescence (TIRF) imaging would provide near-surface field mapping. Near field and stimulated emission depletion (STED) imaging could break the diffraction limit, enabling optical characterization of magnetic fields that vary on submicrometer length scales. Although diamond-based magnetometers are more sensitive, a liquid magnetometer offers several advantages in certain applications: the liquid is inexpensive, conforms to any shaped object, can be completely removed after the measurement, and opens the possibility of using chemistry to tune the magnetic sensitivity and spectral properties of the indicator.

A key challenge in further development of fluorescence-based magnetometry is the development of improved fluorescent indicators. The compounds we tested showed large contrast, but illumination in the near-UV is inconvenient for many applications. Additionally, compound **1** is somewhat photolabile, necessitating a continuous flow during measurements. One would like a compound that is bright, photostable, and excited by visible light. There are no physical prohibitions against such a compound, but to our knowledge one has not yet been identified.

Different applications may also require magnetic field indicators with different dynamic range. The strength of the magnetic field which turns on the fluorescence is determined by the strength of the nuclear hyperfine interactions. Isotopically substituted molecules can have weaker hyperfine couplings, leading to greater sensitivity to small magnetic fields.[35,36] Similarly, in compounds where the electron *g*-factors on the two radical moieties differ by a small amount, reaction outcomes can be sensitive to fields as large as several tesla.[37] Thus by appropriate chemical design, one should be able to map magnetic fields in any desired range.

■ ASSOCIATED CONTENT

Supporting Information. The supporting movie shows a cuvette of **1** illuminated with a 355 nm laser, and placement of a permanent magnet next to the solution leads to a clearly visible increase in fluorescence. This material is available free of charge via the Internet at http://pubs.acs.org.

■ AUTHOR INFORMATION

Corresponding Author
*E-mail: cohen@chemistry.harvard.edu.

■ ACKNOWLEDGMENT

We thank Rohini Shivamoggi, Vijay Jain, Ryan Spoering, Michael Campbell, and Tobias Ritter for help with chemical synthesis. This work was supported by the Defense Advanced Research Projects Agency (DARPA) YFA Grant N66001-091-2104 and the Office of Naval Research (ONR) YIP Grant N000140910868. N.Y. acknowledges the Natural Sciences and Engineering Research Council of Canada (NSERC) for funding his PGS D scholarship. This work was performed in part at the Harvard Center for Nanoscale Systems (CNS), a member of the National Nanotechnology Infrastructure Network (NNIN), which is supported by the National Science Foundation under NSF award no. ECS-0335765.

■ REFERENCES

(1) Chappert, C.; Fert, A.; Van Dau, F. N. *Nat. Mater.* **2007**, *6*, 813.
(2) Lu, A. H.; Salabas, E. L.; Schuth, F. *Angew. Chem., Int. Ed.* **2007**, *46*, 1222.
(3) Yellen, B. B.; Hovorka, O.; Friedman, G. *Proc. Natl. Acad. Sci. U.S.A.* **2005**, *102*, 8860.
(4) Kose, A. R.; Fischer, B.; Mao, L.; Koser, H. *Proc. Natl. Acad. Sci. U.S.A.* **2009**, *106*, 21478.
(5) Bitter, F. *Phys. Rev.* **1931**, *38*, 1903.
(6) Saenz, J. J.; Garcia, N.; Grutter, P.; Meyer, E.; Heinzelmann, H.; Wiesendanger, R.; Rosenthaler, L.; Hidber, H. R.; Guntherodt, H. J. *J. Appl. Phys.* **1987**, *62*, 4293.
(7) Martin, Y.; Wickramasinghe, H. K. *Appl. Phys. Lett.* **1987**, *50*, 1455.
(8) Chang, A. M.; Hallen, H. D.; Harriott, L.; Hess, H. F.; Kao, H. L.; Kwo, J.; Miller, R. E.; Wolfe, R.; van der Zeil, J.; Chang, T. Y. *Appl. Phys. Lett.* **1992**, *61*, 1974.
(9) Kirtley, J. R.; Ketchen, M. B.; Tsuei, C. C.; Sun, J. Z.; Gallagher, W. J.; Yu-Jahnes, L. S.; Gupta, A.; Stawiasz, K. G.; Wind, S. J. *IBM J. Res. Dev.* **1995**, *39*, 655.
(10) Qiu, Z. Q.; Bader, S. D. *Rev. Sci. Instrum.* **2000**, *71*, 1243.
(11) Maertz, B. J.; Wijnheijmer, A. P.; Fuchs, G. D.; Nowakowski, M. E.; Awschalom, D. D. *Appl. Phys. Lett.* **2010**, *96*, 092504.
(12) Pham, L. M.; Le Sage, D.; Stanwix, P. L.; Yeung, T. K.; Glenn, D.; Trifonov, A.; Cappellaro, P.; Hemmer, P. R.; Lukin, M. D.; Park, H.; Yacoby, A.; Walsworth, R. L. *New J. Phys.* **2011**, *13*, 045021.
(13) Schulten, K. *Adv. Solid State Phys.* **1982**, *22*, 61.
(14) Steiner, U. E.; Ulrich, T. *Chem. Rev.* **1989**, *89*, 51.
(15) Timmel, C.; Till, U.; Brocklehurst, B.; McLauchlan, K.; Hore, P. *Mol. Phys.* **1998**, *95*, 71.
(16) Jones, J. A.; Hore, P. J. *Chem. Phys. Lett.* **2010**, *488*, 90.
(17) Khudyakov, I. V.; Arsu, N.; Jockusch, S.; Turro, N. J. *Des. Monomers Polym.* **2003**, *6*, 91.
(18) Turro, N. J. *Proc. Natl. Acad. Sci. U.S.A.* **1983**, *80*, 609.
(19) Turro, N. J. *Modern Molecular Photochemistry*; University Science Books: Mill Valley, CA1991.
(20) Hu, B.; Yan, L.; Shao, M. *Adv. Mater.* **2009**, *21*, 1500.
(21) Blankenship, R. E.; Schaafsma, T. J.; Parson, W. W. *Biochim. Biophys. Acta* **1977**, *461*, 297.

(22) Hoff, A. J.; Rademaker, H.; Van Grondelle, R.; Duysens, L. N. *Biochim. Biophys. Acta* **1977**, *9*, 547.
(23) Maeda, K.; Henbest, K. B.; Cintolesi, F.; Kuprov, I.; Rodgers, C. T.; Liddell, P. A.; Gust, D.; Timmel, C. R.; Hore, P. J. *Nature* **2008**, *453*, 387.
(24) Weller, A.; Staerk, H.; Treichel, R. *Faraday Discuss. Chem. Soc.* **1984**, *78*, 271.
(25) Petrov, N. K.; Borisenko, V. N.; Starostin, A. V.; Alfimov, M. V. *J. Phys. Chem.* **1992**, *96*, 2901.
(26) Yang, N.; Cohen, A. E. *Opt. Express* **2010**, *18*, 25461.
(27) Petrov, N. K.; Shushin, A. I.; Frankevich, E. L. *Chem. Phys. Lett.* **1981**, *82*, 339.
(28) Nath, D. N.; Chowdhury, M. *Pramana* **1990**, *34*, 51.
(29) Cao, H.; Fujiwara, Y.; Haino, T.; Fukazawa, Y.; Tung, C. H.; Tanimoto, Y. *Bull. Chem. Soc. Jpn.* **1996**, *69*, 2801.
(30) Cao, H.; Miyata, K.; Tamura, T.; Fujiwara, Y.; Katsuki, A.; Tung, C. H.; Tanimoto, Y. *J. Phys. Chem. A* **1997**, *101*, 407.
(31) Leslie, S. R.; Fields, A. P.; Cohen, A. E. *Anal. Chem.* **2010**, *82*, 6224.
(32) Lee, H.Supporting Information.
(33) Schuck, P. J.; Fromm, D. P.; Sundaramurthy, A.; Kino, G. S.; Moerner, W. E. *Phys. Rev. Lett.* **2005**, *94*, 7938.
(34) Weller, A.; Nolting, F.; Staerk, H. *Chem. Phys. Lett.* **1983**, *96*, 24.
(35) Werner, H. J.; Staerk, H.; Weller, A. *J. Chem. Phys.* **1978**, *68*, 2419.
(36) Timmel, C. R.; Henbest, K. B. *Philos. Trans. R. Soc., A* **2004**, *362*, 2573.
(37) Wakasa, M.; Nishizawa, K.; Abe, H.; Kido, G.; Hayashi, H. *J. Am. Chem. Soc.* **1999**, *121*, 9191.